J. Fluid Mech. (2021), *vol*. 915, A14, doi:10.1017/jfm.2021.58

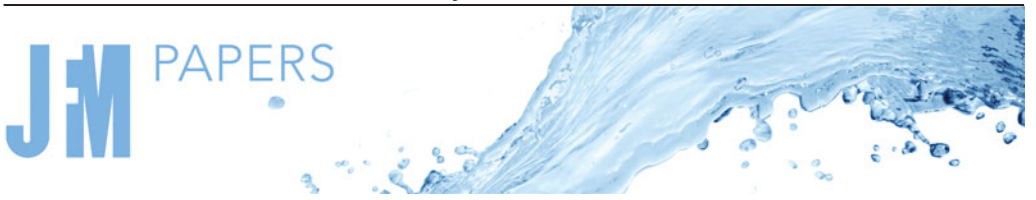

Stabilizing/destabilizing the large-scale circulation in turbulent Rayleigh–Bénard convection with sidewall temperature control

Shengqi Zhang[1], Xin Chen[2], Zhenhua Xia[3],†, Heng-Dong Xi[2], Quan Zhou[4] and Shiyi Chen[1,5],†

[1]State Key Laboratory for Turbulence and Complex Systems, Peking University, Beijing 100871, PR China

[2]Institute of Extreme Mechanics and School of Aeronautics, Northwestern Polytechnical University, Xi'an 710072, PR China

[3]Department of Engineering Mechanics, Zhejiang University, Hangzhou 310027, PR China

[4]Shanghai Key Laboratory of Mechanics in Energy Engineering, Shanghai Institute of Applied Mathematics and Mechanics, School of Mechanics and Engineering Science, Shanghai University, Shanghai 200072, PR China

[5]Department of Mechanics and Aerospace Engineering, Southern University of Science and Technology, Shenzhen 518055, PR China

(Received 16 June 2020; revised 6 October 2020; accepted 15 January 2021)

In this paper, we designed two different configurations with locally isothermal sidewalls, where the temperature is set to be the bulk temperature, to control the large-scale circulation in turbulent Rayleigh–Bénard convection, namely two-point control and four-point control. At fixed Rayleigh number $Ra = 10^8$ and Prandtl number $Pr = 2$, a series of direct numerical simulations are performed on both two-dimensional (2-D) and quasi-two-dimensional (quasi-2-D) cavities with both types of control, where the width of the control area is fixed at $\delta_c = 0.05$ and the vertical distance from the cavity centre h_c varies from 0 to 0.45 with an interval of 0.05. Our results show that the control effect depends on h_c, the control configurations as well as the flow dimensions. For 2-D cavities, both two-point control and four-point control suppress the flow reversal when $h_c \geq 0.05$, accompanied by the enhancement of vertical heat transfer and the strength of the large-scale circulation. For quasi-2-D cavities, the suppression of the flow reversals is obvious with two-point control and $h_c \geq 0.05$, while the effect is rather limited with four-point control. Further experiments with $Pr = 5.7$ and Ra up to 7.36×10^8 show that two-point control with $h_c = 0.15$ can effectively suppress the flow reversal, while two-point control with $h_c = 0$ can suppress the reversals at low $Ra = 1.93 \times 10^8$ and activate them at higher $Ra = 7.36 \times 10^8$, which agrees well with our numerical simulations.

Key words: Bénard convection

† Email addresses for correspondence: xiazh@zju.edu.cn, chensy@sustech.edu.cn

1. Introduction

Buoyancy-driven convection is one of the key problems in a wide range of flows, including atmospheric convection (Hartmann, Moy & Fu 2001), ocean convection (van Doorn *et al.* 2000) and geophysical convection (Glatzmaiers & Roberts 1995). In buoyancy-driven convection, the flow obtains kinetic energy from its potential energy, which will spontaneously trigger and generate turbulence under certain conditions even without direct forcing, and the resulting flow exhibits complex phenomena due to the coupling of velocity and density. Owing to its simplicity in geometry and governing equation, Rayleigh–Bénard convection (RBC) is regarded as a canonical model representing buoyancy-driven convection for understanding, predicting and even controlling various scientific and application problems (Ahlers, Grossmann & Lohse 2009; Lohse & Xia 2010). In addition to the scalings of heat transfer and kinetic energy, which were successfully explained by Grossmann–Lohse (GL) theory (Grossmann & Lohse 2000, 2001, 2002; Ahlers *et al.* 2009; Lohse & Xia 2010), there are other fascinating flow behaviours in RBC, and large-scale circulation (LSC) and its reversal are among them (Benzi 2005; Brown & Ahlers 2007, 2008*b*; Assaf, Angheluta & Goldenfeld 2011; Petschel *et al.* 2011; Vasil'ev & Frick 2011; Wagner & Shishkina 2013; Chen, Wang & Xi 2020). In the past, flow reversals have been reported in cylindrical cells, two-dimensional (2-D) cavities as well as quasi-two-dimensional (quasi-2-D)/three-dimensional (3-D) cavities experimentally and numerically (Cioni, Ciliberto & Sommeria 1997; Brown, Nikolaenko & Ahlers 2005; Sun, Xi & Xia 2005; Tsuji *et al.* 2005; Xi & Xia 2007, 2008).

A comprehensive study was performed by Sugiyama *et al.* (2010), through both experiments and numerical simulations, to quantify the existence and frequency of flow reversals in 2-D and quasi-2-D geometry with a wide range of Rayleigh number Ra and Prandtl number Pr (for definitions, see § 2.1). A phase diagram about the occurrence of flow reversals and the corresponding statistical results of reversal frequency were presented, together with a discussion on the dynamics of reversals. By introducing a Fourier decomposition, Chandra & Verma (2011) studied the dynamics and symmetries of the flow reversals in 2-D RBC and observed that the amplitude of one of the large-scale modes almost vanishes while another mode rises sharply during the reversals. Chandra & Verma (2013) further examined the mechanism of the flow reversals in 2-D RBC and argued that the vortex reconnection of two attracting corner rolls, which have the same sign of vorticity, will lead to major restructuring of the LSC and flow reversal. Castillo-Castellanos *et al.* (2019) identified two different types of flow regimes, i.e. consecutive flow reversals and extended cessations, for $Ra = 10^6$ to 5×10^8 and $Pr = 3$ and 4.3, and used proper orthogonal decomposition and cluster-based analysis to investigate the flow modes in the two regimes. Besides analysis mainly based on simulations and experiments, there are some other works trying to capture the key mechanisms of reversals with stochastic (Sreenivasan, Bershadskii & Niemela 2002) or deterministic (Araujo, Grossmann & Lohse 2005) models in the form of ordinary differential equations. Other recent works presenting theoretical and numerical investigations on flow reversals include, but are not limited to, Ni, Huang & Xia (2015), Podvin & Sergent (2015), Chong *et al.* (2018) and Chen *et al.* (2019).

In addition to the studies on RBC with classic set-ups, new flow set-ups are also introduced, including rough walls, varying fluid properties, and different velocity or temperature boundary conditions (Qiu, Xia & Tong 2005; Wang *et al.* 2017; Zhang *et al.* 2018; Zhu *et al.* 2019). These new set-ups may significantly influence flow structures, statistics and reversal behaviours. Huang *et al.* (2015) introduced the mixed boundary

condition with one horizontal plate having fixed heat flux and they observed a decrease of reversal frequency as compared to the classic set-up with fixed temperature, suggesting that the reduction of symmetry may reduce the motivation of LSC to reverse. Xia *et al.* (2016) applied the low-Mach-number equation in the simulation of RBC to investigate the non-Oberbeck–Boussinesq effect and discovered different reversal properties. Wang *et al.* (2018) investigated the flow reversals in 2-D cells with aspect ratio $\Gamma = 1$ (where $\Gamma =$ width/height) and managed to efficiently suppress reversals by tilting the cavity. Chen *et al.* (2020) defined and identified reversals led by LSC and corner rolls separately, and reported that the total reversal frequency in a corner-less cell, where corner vortices are absent and the reversal is main-vortex-led, has the same piecewise scaling law and transition behaviour as that in a normal cell, where both main-vortex-led and corner-vortex-led reversals exist. Furthermore, they showed that the frequency of main-vortex-led reversals in a normal cell is in excellent agreement with that in a corner-less cell. Other interesting findings and analysis of the non-classic set-up can be found in Sun *et al.* (2005), Brown & Ahlers (2008*a*), Stevens, Lohse & Verzicco (2014), Wang *et al.* (2017), Wan *et al.* (2019) and Wang, Zhou & Sun (2020).

Recently, Zhang *et al.* (2020) introduced a small constant-temperature region on both sidewalls in a 2-D square cavity. Direct numerical simulation results showed that effective suppression or activation of flow reversals can be realized with the proper location and size of the control regions. However, the work was limited to 2-D simulation results. In this paper, we extend the former work to quasi-2-D cases. In addition, a more symmetric control configuration with two control regions on each sidewall is also introduced, and the results are compared with the previous control configuration with one control region on each sidewall. The present paper is organized as follows. We first describe the basic equations along with numerical and experimental set-ups in § 2. The results and discussion related to the simulations at $Ra = 10^8$ and $Pr = 2$ are presented in § 3. Experimental results and direct numerical results at higher Ra are shown in § 4 in order to examine the realizability of control and further support the conclusions. Finally, § 5 will summarize the present work.

2. Basic set-ups

2.1. *Governing equations and boundary conditions*

In this paper, we consider turbulent RBC with Boussinesq approximation in 2-D and 3-D (quasi-2-D) geometry. The origin of the coordinates is defined at the centre of the cavity. For the 2-D cases, the cavity height $\hat{H}$ (y direction) and length $\hat{L}$ (x direction) are the same, i.e. aspect ratio $\Gamma = \hat{L}/\hat{H} = 1$; for the quasi-2-D cases, the width of the cavity is $\hat{W} = 0.3\hat{H}$ (z direction). $\hat{\boldsymbol{u}} = (\hat{u}, \hat{v}, \hat{w})$ is the velocity, with $\hat{u}$, $\hat{v}$ and $\hat{w}$ being the velocity components in the x, y and z (if it exists) directions, respectively; $\hat{\theta}$ is the temperature; $\hat{\theta}_l$ and $\hat{\theta}_u$ are the constant temperatures at the lower and upper walls, respectively; $\hat{\theta}_0 = (\hat{\theta}_l + \hat{\theta}_u)/2$ is the bulk temperature; and $\Delta\hat{\theta} = \hat{\theta}_l - \hat{\theta}_u$. The background temperature outside the sidewalls is set to $\hat{\theta}_0$. We define $\hat{\nu}$ as the kinematic viscosity, $\hat{\kappa}$ as the thermal diffusivity, $\hat{\lambda}$ as the thermal conductivity, $\hat{g}$ as the gravitational acceleration and $\hat{\beta}$ as the thermal expansion coefficient.

The free-fall velocity and the free-fall time can then be defined as $\hat{U} = (\hat{g}\hat{\beta}\Delta\hat{\theta}\hat{H})^{1/2}$ and $\hat{T} = \hat{H}/\hat{U}$, respectively. With velocity, time, length and temperature scales chosen as

$\hat{U}$, $\hat{T}$, $\hat{H}$ and $\Delta\hat{\theta}$, respectively, and with $\theta \triangleq (\hat{\theta} - \hat{\theta}_0)/\Delta\hat{\theta}$, the governing equations and related boundary conditions can be non-dimensionalized as follows:

$$\left.\begin{gathered}
\boldsymbol{\nabla}\cdot\boldsymbol{u} = 0, \\
\frac{\partial \boldsymbol{u}}{\partial t} + \boldsymbol{u}\cdot\boldsymbol{\nabla}\boldsymbol{u} = -\boldsymbol{\nabla} p + \frac{1}{\sqrt{Ra/Pr}}\nabla^2\boldsymbol{u} + \theta\boldsymbol{j}, \\
\frac{\partial \theta}{\partial t} + \boldsymbol{u}\cdot\boldsymbol{\nabla}\theta = \frac{1}{\sqrt{Ra\,Pr}}\nabla^2\theta, \\
y = \pm 0.5\text{:}\quad \boldsymbol{u} = 0, \quad \theta = \mp 0.5, \\
x = -0.5\text{:}\quad \boldsymbol{u} = 0, \quad (\theta - \theta_0) - R_l\partial\theta/\partial x = 0, \\
x = 0.5\text{:}\quad \boldsymbol{u} = 0, \quad (\theta - \theta_0) + R_r\partial\theta/\partial x = 0, \\
z = \pm 0.15\text{:}\quad \boldsymbol{u} = 0, \quad \partial\theta/\partial z = 0 \quad \text{(quasi-2-D)}.
\end{gathered}\right\} \tag{2.1}$$

Here, the Rayleigh number is $Ra = \hat{g}\hat{\beta}\Delta\hat{\theta}\hat{H}^3/(\hat{\nu}\hat{\kappa})$, the Prandtl number is $Pr = \hat{\nu}/\hat{\kappa}$, the normalized bulk temperature is $\theta_0 = 0$, and the normalized thermal resistances are $R_l(y) = \hat{\lambda}\hat{R}_l(\hat{y})\hat{H}^{-1}$ and $R_r(y) = \hat{\lambda}\hat{R}_r(\hat{y})\hat{H}^{-1}$, where $\hat{R}_l(\hat{y})$ and $\hat{R}_r(\hat{y})$ are the thermal resistance per unit area at the left and right sidewalls, respectively. It is easy to see that $R_l(y)$ and $R_r(y)$ control the thermal boundary condition on the sidewalls. If $R_l(y) = R_r(y) = \infty$, the above governing equations correspond to the classic set-up with adiabatic left and right sidewalls, i.e. $\partial\theta/\partial x = 0$ on the left and right sidewalls. Furthermore, $R_l(y_0) = 0$ can lead to a local isothermal boundary condition with $\theta = \theta_0$. Zhang *et al.* (2020) introduced a local $R_l(y) = 0$ region on the left sidewall and a local $R_r(y) = 0$ region on the right sidewall, as shown in figure 1(*a*), and the coefficients governing the temperature conditions on the sidewalls are

$$R_l(y) = \begin{cases} 0, & |y - h_c| < \delta_c/2, \\ \infty, & |y - h_c| \geq \delta_c/2, \end{cases} \quad \text{and} \quad R_r(y) = \begin{cases} 0, & |y + h_c| < \delta_c/2, \\ \infty, & |y + h_c| \geq \delta_c/2. \end{cases} \tag{2.2a,b}$$

We denote the configuration with coefficients (2.2*a*,*b*) as the two-point control configuration. It should be noted that the formulations of the boundary condition on the left and right sidewalls are different from those used in Zhang *et al.* (2020), where they used two control parameters to simply combine the isothermal and adiabatic boundary conditions together. Here, we introduce the thermal resistance and the formulae for the boundary conditions are of clear physical meaning.

In addition, a new configuration with two control regions on each (left/right) sidewall is introduced and R_l and R_r are defined as

$$R_l(y) = R_r(y) = \begin{cases} 0, & ||y| - h_c| < \delta_c/2, \\ \infty, & ||y| - h_c| \geq \delta_c/2. \end{cases} \tag{2.3}$$

This new symmetric configuration is shown in figure 1(*b*) and it is denoted as the four-point control configuration. It is seen that, with $h_c = 0$, the two-point control and the four-point control are the same.

2.2. *Numerical set-up*

For both 2-D and quasi-2-D simulations, the second-order finite difference code AFiD (Van Der Poel *et al.* 2015) is used with some modifications, where the discretized Poisson

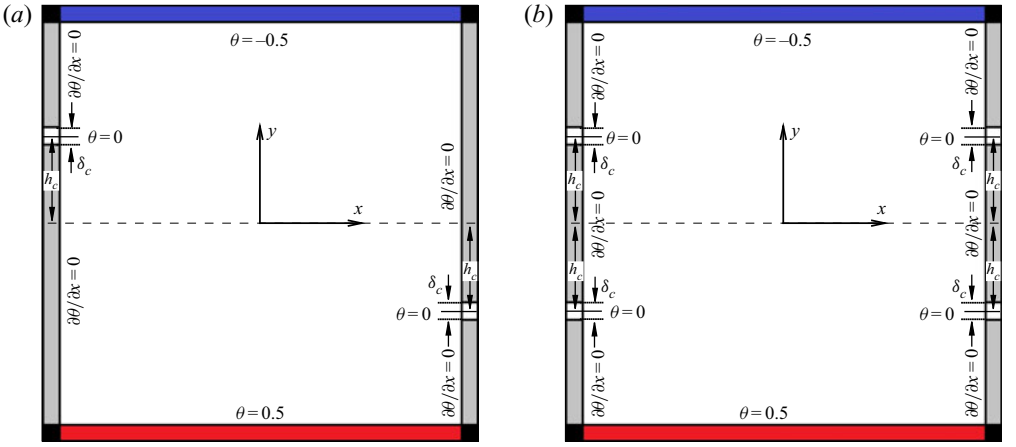

Figure 1. Sketches of sidewall controlled 2-D RBC with $h_c > 0$: (*a*) two-point control and (*b*) four-point control. In quasi-2-D RBC, the z direction points out from the paper and adiabatic conditions are applied on both sidewalls in the z direction.

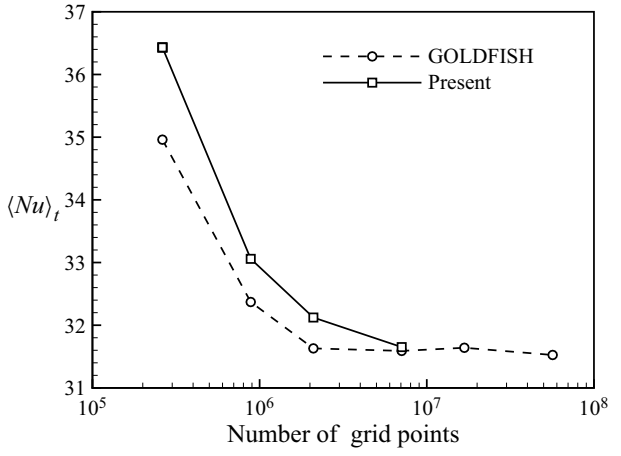

Figure 2. Plot of $\langle Nu\rangle_t$ in a cubic RBC cell at $Ra = 1 \times 10^8$ and $Pr = 1$ obtained using the present code with different numbers of grid points. The results reported in Kooij *et al.* (2018) from the validated code GOLDFISH are also shown for comparison.

equation is decoupled using a discrete cosine transform in horizontal directions and solved with a tridiagonal solver, while the time marching is realized with the second-order explicit Adams–Bashforth scheme. Figure 2 shows the time-averaged Nusselt number $\langle Nu\rangle_t$ (see the definition below) obtained using the present code with different numbers of grid points in a cubic RBC cell at $Ra = 1 \times 10^8$ and $Pr = 1$. The results shown in Kooij *et al.* (2018) from another validated code GOLDFISH are also included as reference. It is seen that the $\langle Nu\rangle_t$ computed with the present code could converge to an accurate value with increasing number of grid points, indicating the correctness of the present code.

In this paper, the widths of the control regions are kept the same and they are fixed as $\delta_c = 0.05$. We mainly focus on the cases at $Ra = 10^8$ and $Pr = 2$, where both 2-D and quasi-2-D simulations are performed with the two-point control configuration, the four-point control configuration, as well as the classic adiabatic configuration (no control).

Dimension	Control configuration	h_c	t_E	Sampling time/t_E	Reversals	$\frac{\langle\tau\rangle}{100t_E}$
2-D	No	—	6.54	4000	41	0.935 ± 0.12
2-D	Two-point	0	6.51	4000	12	3.2 ± 0.59
2-D	Two-point	0.05	7.26	4000	0	—
2-D	Two-point	0.1	7.95	4000	0	—
2-D	Two-point	0.15	8.65	4000	0	—
2-D	Two-point	0.2	9.31	4000	0	—
2-D	Two-point	0.25	8.82	4000	0	—
2-D	Two-point	0.3	8.94	4000	0	—
2-D	Two-point	0.35	9.51	4000	0	—
2-D	Two-point	0.4	9.62	4000	0	—
2-D	Two-point	0.45	7.58	4000	12	2.81 ± 1.4
2-D	Four-point	0.05	7.04	140 000	22	63 ± 12
2-D	Four-point	0.1	7.75	4000	0	—
2-D	Four-point	0.15	8.4	4000	0	—
2-D	Four-point	0.2	8.67	4000	0	—
2-D	Four-point	0.25	8.13	4000	0	—
2-D	Four-point	0.3	8.44	4000	0	—
2-D	Four-point	0.35	8.9	4000	0	—
2-D	Four-point	0.4	8.96	4000	0	—
2-D	Four-point	0.45	7.26	4000	21	1.72 ± 0.24
Quasi-2-D	No	—	10.2	3500	55	0.629 ± 0.080
Quasi-2-D	Two-point	0	10.1	3500	56	0.597 ± 0.076
Quasi-2-D	Two-point	0.05	10.2	3500	42	0.851 ± 0.13
Quasi-2-D	Two-point	0.1	10.5	3500	18	1.9 ± 0.52
Quasi-2-D	Two-point	0.15	10.5	3500	21	1.62 ± 0.50
Quasi-2-D	Two-point	0.2	10.8	3500	18	1.9 ± 0.28
Quasi-2-D	Two-point	0.25	10.8	3500	12	2.15 ± 0.77
Quasi-2-D	Two-point	0.3	10.7	3500	8	4.26 ± 2.9
Quasi-2-D	Two-point	0.35	10.6	3500	8	4.74 ± 2.2
Quasi-2-D	Two-point	0.4	10.7	5000	8	6.55 ± 2.8
Quasi-2-D	Two-point	0.45	10.9	3500	0	—
Quasi-2-D	Four-point	0.05	10.2	3500	54	0.607 ± 0.075
Quasi-2-D	Four-point	0.1	10.2	3500	40	0.877 ± 0.12
Quasi-2-D	Four-point	0.15	10.3	3500	39	0.914 ± 0.12
Quasi-2-D	Four-point	0.2	10.3	3500	54	0.646 ± 0.090
Quasi-2-D	Four-point	0.25	10.3	3500	33	1.01 ± 0.27
Quasi-2-D	Four-point	0.3	10.3	3500	41	0.859 ± 0.11
Quasi-2-D	Four-point	0.35	10.2	3500	52	0.673 ± 0.11
Quasi-2-D	Four-point	0.4	10.2	3500	47	0.746 ± 0.12
Quasi-2-D	Four-point	0.45	10.3	3500	51	0.685 ± 0.085

Table 1. Parameters of the 2-D and quasi-2-D simulations with $Ra = 10^8$ and $Pr = 2$.

For the two-point control configuration, h_c varies in $[0, 0.45]$ with an increment of 0.05, while for the four-point control configuration h_c varies in $[0.05, 0.45]$ with the same increment of 0.05. For comparison with the experimental results, we perform quasi-2-D simulations at $Ra = 1.93 \times 10^8$ and $Pr = 5.7$ with two-point $h_c \in \{0, 0.15\}$ control and without control, and also at $Ra = 7.36 \times 10^8$ and $Pr = 5.7$ with $h_c = 0$ control and without control. The parameters of the simulations are listed in table 1.

For the 2-D simulations, the grid size is 192×192. For the quasi-2-D simulations, the mesh is $192 \times 192 \times 64$ at $Ra = 10^8$ and $Ra = 1.93 \times 10^8$ and it is $256 \times 256 \times 72$

at $Ra = 7.36 \times 10^8$. For all the simulation cases, the mesh is uniform in the horizontal directions (x and z directions) while it is refined near the walls in the vertical direction (y direction) to make sure that the grid size $\hat{\Delta}$ satisfies $\hat{\Delta} < 0.6 \min[\widehat{\eta_K}, \widehat{\eta_B}]$ in the boundary layers. The numbers of grid points in the x and y directions for the $Ra = 10^8$ simulations are the same as in the present validation case with the largest grid size. Here $\widehat{\eta_K} = [\hat{\nu}^3/\hat{\varepsilon}(\hat{\boldsymbol{x}}, \hat{t})]^{1/4}/\hat{H}$ (with $\hat{\varepsilon}(\hat{\boldsymbol{x}}, \hat{t})$ being the local turbulent dissipation) is the local Kolmogorov scale and $\widehat{\eta_B} = \widehat{\eta_K} Pr^{-1/2}$ is the Batchelor scale. The time steps are small enough to make sure that the Courant–Friedrichs–Lewy numbers are smaller than 0.2.

For convenience in expression, any 2-D field $\phi(x, y, t)$ could be rewritten as $\phi(x, y, z, t)$ with the extra dimension being trivial with $\partial\phi/\partial z \equiv 0$, and we could also define $w \equiv 0$. In the following, $\langle\cdot\rangle_t$, $\langle\cdot\rangle_x$, $\langle\cdot\rangle_y$ and $\langle\cdot\rangle_z$ denote the averages in time, along the x axis, along the y axis and along the z axis, respectively; and $\langle\cdot\rangle_V$ denotes the volume average. Following the definition in Sugiyama *et al.* (2010), the LSC turnover time t_E in both 2-D and quasi-2-D simulation cases is defined as $t_E = 4\pi/\langle|\omega_z(0, 0, 0, t)|\rangle_t$, where $\omega_z(0, 0, 0, t)$ is the central vorticity in the z direction. The reversal indicator is defined as the volume-averaged angular momentum

$$L(t) = \langle xv - yu\rangle_V. \tag{2.4}$$

The value $L < 0$ usually corresponds to a clockwise LSC and *vice versa*, which is the same as in Zhang *et al.* (2020). All simulations are run for more than $2500t_E$ in order to obtain reasonable estimations on the reversal interval and flow statistics.

2.3. *Experimental set-up*

We also perform experiments to measure of the LSC at higher Ra for the two-point control configuration. The experimental set-up used here is almost the same as that in Chen *et al.* (2019), with the size of the fluid region being $\hat{H} = \hat{L} = 12.6$ cm and $\hat{W} = 3.8$ cm $\approx 0.3\hat{H}$. The fluid is bounded with vertical walls mainly made of Plexiglas and horizontal plates made of copper. A refrigerated circulator (PolyScience) and two resistive film heaters are used to maintain isothermal boundary conditions at the top and bottom plates, respectively. A locally isothermal boundary condition on the sidewalls is realized with inserted copper blocks (of size $\delta_c = 0.05\hat{H}$) conducting heat between the air and the working fluid, while the fluid–solid interface is kept flat. During the experiment, the convection cell is put in a thermostatic box with its interior temperature regulated at 28 °C. Deionized water is chosen as the working fluid. As a result, the Pr of the working fluid is 5.7. Six thermistors are embedded in the bottom plate at approximately 8 mm below the fluid–solid interface, with horizontal coordinates $\hat{x} = 0, \pm\hat{L}/4$ and $\hat{z} = \pm 5$ mm, respectively. The temperature obtained from the two thermistors on the left ($\hat{x} = -\hat{L}/4,\ \hat{z} = \pm 5$ mm) are denoted as $\hat{\theta}_{left}$, and the temperature obtained from the two thermistors on the right ($\hat{x} = \hat{L}/4,\ \hat{z} = \pm 5$ mm) are denoted as $\hat{\theta}_{right}$. There are another six thermistors embedded in the top plate with the same configuration. In order to test the capability of the copper blocks to realize the isothermal boundary condition, a thermistor is embedded in the centre of a copper block in a test case with $Ra = 1.93 \times 10^8$ and two-point $h_c = 0.15$ control. The temperature of the copper block fluctuates with a mean of 28.32 °C and a root-mean-square (r.m.s.) value of 1.35×10^{-2} °C, indicating that copper blocks can achieve a local isothermal boundary condition with bulk temperature approximately.

Method	Control configuration	$\frac{Ra}{10^8}$	h_c	t_E	Sampling time/t_E	Reversals	$\frac{\langle\tau\rangle}{100t_E}$
Simulation	No	1.93	—	14.9	2500	74	0.332 ± 0.037
Simulation	Two-point	1.93	0	15.1	2500	59	0.42 ± 0.051
Simulation	Two-point	1.93	0.15	14.8	2500	10	2.71 ± 1.2
Simulation	No	7.36	—	13.3	4000	5	5.52 ± 2.0
Simulation	Two-point	7.36	0	13.1	3500	6	2.72 ± 0.86
Experiment	Two-point	1.37	0.15	29.5	1500	34	0.385 ± 0.071
Experiment	Two-point	1.92	0	31.1	1500	47	0.312 ± 0.036
Experiment	Two-point	1.93	0.15	28.5	2200	12	1.72 ± 0.59
Experiment	Two-point	2.71	0	30.5	2800	40	0.702 ± 0.10
Experiment	Two-point	2.71	0.15	28.7	3000	22	0.769 ± 0.20
Experiment	Two-point	5.56	0	30.1	4500	17	2.41 ± 0.51
Experiment	Two-point	7.36	0	29.9	4800	10	3.99 ± 1.4

Table 2. Parameters of simulations and experiments with $Ra > 10^8$ and $Pr = 5.7$. The t_E value is estimated differently in simulations and experiments.

In the experiments, h_c is chosen to be 0 and 0.15. For $h_c = 0$, measurements are performed with $Ra = 1.92 \times 10^8$, 2.71×10^8, 5.56×10^8 and 7.36×10^8. For $h_c = 0.15$, measurements are carried out with $Ra = 1.37 \times 10^8$, 1.93×10^8 and 2.71×10^8. The parameters of the experiments are given in table 2. For the experimental cases, the LSC turnover time is obtained by the cross-correlation of the measured temperature signals inside the bottom plates following Brown, Funfschilling & Ahlers (2007). All measurements are performed for over $1500t_E$ for estimation of reversal intervals and statistics. Here, t_E is estimated based on the cross-correlation of the temperature signals inside the plates, and data for the no-control experimental cases are obtained from the previous experiments described in Chen *et al.* (2019). The reversal indicator (or flow strength) is chosen as the temperature difference measured between the right and left thermistors in the bottom plate:

$$\hat{\delta}(t) = \hat{\theta}_{right} - \hat{\theta}_{left}. \tag{2.5}$$

A value $\hat{\delta} < 0$ usually corresponds to a clockwise LSC and *vice versa*, which is in accordance with Chen *et al.* (2019).

2.4. *Reversal detection*

In this section, $\xi(t)$ is used to represent the generic reversal indicator, which represents $L(t)$ in simulations and $\hat{\delta}(t)$ in the experiments, for simplicity. In order to identify the reversal events with the time series of $\xi(t)$, the criterion of reversals proposed by Huang & Xia (2016) is adapted here with small changes. According to Huang & Xia (2016), the probability density function (p.d.f.) of ξ for traditional no-control cases should have two distinct peaks, and a double-Gaussian fit could be applied to identify the locations of the two peaks as $\xi^{(-)}$ and $\xi^{(+)}$, which are then defined as thresholds for the starting or ending of reversals. However, with proper set-ups in two-point control configuration, the system may strongly prefer a clockwise LSC over an anticlockwise one, resulting in a decreasing height of the peak in $\xi > 0$. Generally, if the peak in $\xi > 0$ can still be discerned, then the

locations of the peaks can be chosen as $\xi^{(-)}$ and $\xi^{(+)}$, respectively. In some cases, when the peak in $\xi > 0$ disappears, $\xi^{(+)}$ should be chosen as $-\xi^{(-)}$, with $\xi^{(-)}$ being the location of the peak in $\xi < 0$. The rest of the criterion is the same as introduced in Huang & Xia (2016). For example, if the LSC reverses from anticlockwise state to clockwise state, $\xi(t)$ should shift from $\xi < \xi^{(-)}$ to $\xi > \xi^{(+)}$ and remain larger than $\xi^{(-)}$ for at least t_E before reversing back.

When the reversal criterion is defined, we can then quantitatively characterize the flow reversal. Following Sugiyama *et al.* (2010), τ is used to denote the time interval between two successive reversals, and $\langle\tau\rangle$, the mean time interval between successive reversals, can represent the reversal feature for a general RBC system where it does not prefer any LSC orientation. However, as mentioned above and verified in Zhang *et al.* (2020) and below, the controlled system with the symmetry-broken two-point control configuration ($h_c > 0$) may prefer certain LSC orientation, and thus the reversal activity could be characterized more delicately. We use τ_- to denote the time interval between an 'anticlockwise to clockwise' reversal and a successive 'clockwise to anticlockwise' reversal. Accordingly, τ_+ denotes the time interval between a 'clockwise to anticlockwise' reversal and a successive 'anticlockwise to clockwise' reversal. In other words, τ_- and τ_+ are the time span of the system when it is in the clockwise state and anticlockwise state, respectively, between two successive reversals; N_- and N_+ denote the numbers of detected τ_- and τ_+ respectively; and $\langle\tau_-\rangle$ and $\langle\tau_+\rangle$ denote the average of detected τ_- and τ_+, respectively. Thus, one can write

$$\langle\tau_-\rangle = \frac{1}{N_-}\sum_{i=1}^{N_-}\tau_{-,i}, \quad \langle\tau_+\rangle = \frac{1}{N_+}\sum_{i=1}^{N_+}\tau_{+,i}. \tag{2.6a,b}$$

The error bars of $\langle\tau_-\rangle$ and $\langle\tau_+\rangle$ are the standard deviations $\sqrt{\langle(\tau_- - \langle\tau_-\rangle)^2\rangle/N_-}$ and $\sqrt{\langle(\tau_+ - \langle\tau_+\rangle)^2\rangle/N_+}$, respectively. The mean value of the two kinds of time intervals is defined as $\langle\tau\rangle \triangleq (\langle\tau_-\rangle + \langle\tau_+\rangle)/2$ with error bar quantified using $\sqrt{\langle(\tau_- - \langle\tau_-\rangle)^2\rangle/N_- + \langle(\tau_+ - \langle\tau_+\rangle)^2\rangle/N_+}/2$. It should be noted that, when the system does not prefer any LSC orientation, $N_- \approx N_+$ and $\langle\tau_-\rangle \approx \langle\tau_+\rangle$, the above definitions of $\langle\tau\rangle$ and its error bar will be degenerated to their traditional definitions.

3. Numerical results at $Ra = 10^8$ and $Pr = 2$

3.1. *Suppression/activation of reversals*

In the previous work, Zhang *et al.* (2020) showed that two-point control with different h_c and δ_c can either suppress or enhance the flow reversals in a 2-D cavity at different Ra and Pr. In this subsection, we will focus on the influences of the two-point and four-point control configurations on the flow reversals in 2-D and quasi-2-D cavities at $Ra = 10^8$ and $Pr = 2$ when $\delta_c = 0.05$ is fixed.

Figure 3 shows the time series of $L(t)$ from six different 2-D simulations at $Ra = 10^8$ and $Pr = 2$. When there is no control on the sidewalls, flow reversals happen frequently and randomly, as shown in figure 3(*a*). The system does not prefer a certain LSC orientation, and $\langle\tau\rangle_0 \approx \langle\tau_-\rangle \approx \langle\tau_+\rangle = 93.5 \pm 12t_E$. We take this $\langle\tau\rangle_0$ as a reference. When the two-point control is applied at the centre of the sidewalls, i.e. $h_c = 0$, as displayed in figure 3(*b*), flow reversals can still be observed. However, the number of reversal events

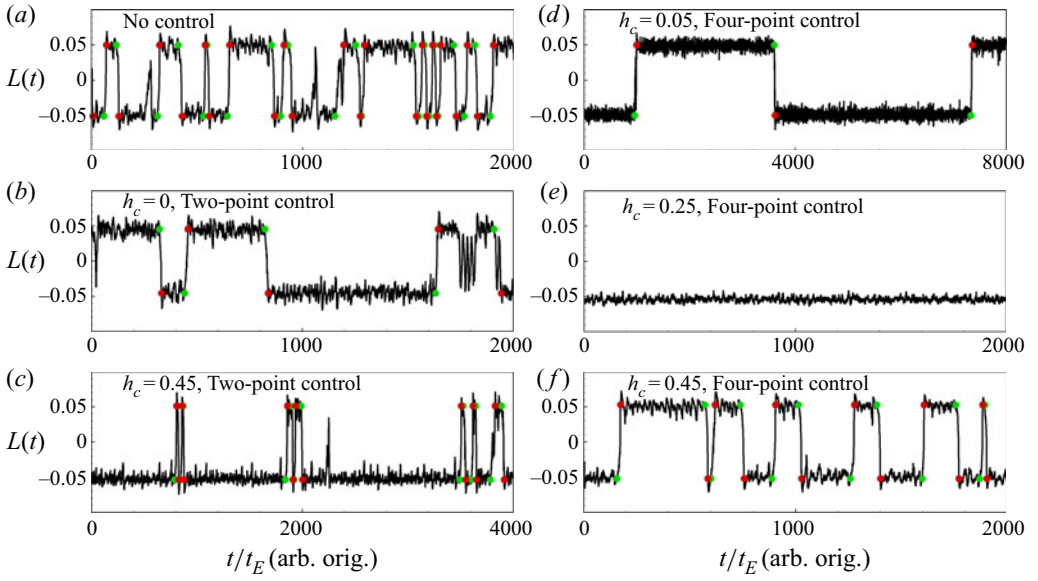

Figure 3. Time series $L(t)$ of 2-D simulations at $Ra = 10^8$ and $Pr = 2$: (*a*) no control; (*b*) two-point control with $h_c = 0$; (*c*) two-point control with $h_c = 0.45$; (*d*) four-point control with $h_c = 0.05$; (*e*) four-point control with $h_c = 0.25$; and (*f*) four-point control with $h_c = 0.45$. The origins of time are chosen differently for each case (arb. orig.). Green and red circles represent reversal starts and ends, respectively.

reduces very obviously as compared to the no-control case. Although the system still does not favour a certain LSC orientation due to the fact that the control is symmetric, it can stay in a certain state for much longer time, resulting in much larger $\langle\tau\rangle$. Nevertheless, when the location of the two-point control moves away from the centre, the symmetry of the system is broken and it prefers the clockwise state with $h_c > 0$. When $0.05 \leq h_c \leq 0.4$, the flow reversal is entirely eliminated, as listed in table 1. For an extreme case with $h_c = 0.45$, as depicted in figure 3(*c*), although flow reversals still happen, the system will reverse back very soon and stay in the clockwise state for most of the time. In this case, $\langle\tau_-\rangle$ is much larger than $\langle\tau\rangle_0$ while $\langle\tau_+\rangle$ is much smaller than $\langle\tau\rangle_0$, but the overall mean value of the time intervals $\langle\tau\rangle$ is still larger than $\langle\tau\rangle_0$, indicating that the sidewall control can still suppress the flow reversal. For the symmetric four-point control configuration, the sidewall control can still suppress the flow reversal (see the values of $\langle\tau\rangle$ in table 1), and the flow reversal events occur much less frequently, as shown in figure 3(*d*) with $h_c = 0.05$ and in figure 3(*f*) with $h_c = 0.45$, and no reversal can be observed for $h_c = 0.25$, as shown in figure 3(*e*).

Figure 4 shows the time series of $L(t)$ from six different quasi-2-D simulations at $Ra = 10^8$ and $Pr = 2$. For the no-control case shown in figure 4(*a*), we can observe the frequently and randomly occurring flow reversals, and $\langle\tau\rangle_0 \approx 62.9 \pm 8.0t_E$. Different from the 2-D results, the two-point control with $h_c = 0$ has little effect on controlling the flow reversals, $\langle\tau\rangle \approx 59.7 \pm 7.6t_E$, and no clear conclusion can be made from figure 4(*b*). When h_c increases, $\langle\tau\rangle$ increases and the system favours the clockwise LSC. For $h_c = 0.3$ as shown in figure 4(*c*), we can only observe two flow reversals for a time span $2000t_E$ and the system is at the clockwise LSC state for more than $1950t_E$. When h_c further increases to 0.45, the flow reversals are fully suppressed, as listed in table 1. For the four-point control configuration, the control effect is much weaker. For $h_c = 0.05$ shown in

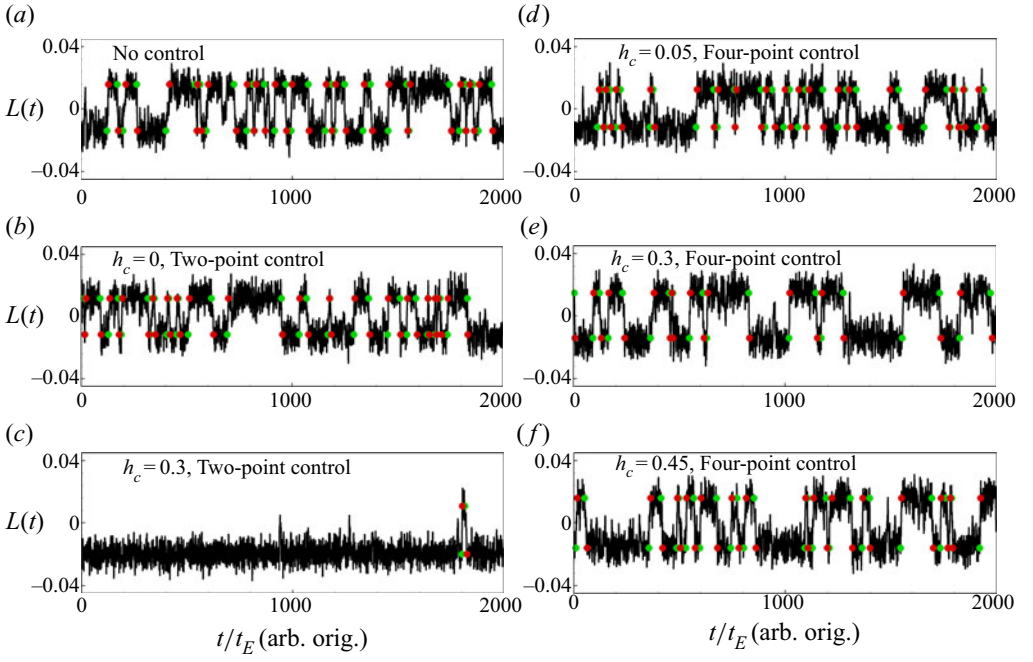

Figure 4. Time series $L(t)$ of quasi-2-D simulations at $Ra = 10^8$ and $Pr = 2$: (*a*) no control; (*b*) two-point control with $h_c = 0$; (*c*) two-point control with $h_c = 0.3$; (*d*) four-point control with $h_c = 0.05$; (*e*) four-point control with $h_c = 0.3$; and (*f*) four-point control with $h_c = 0.45$. The origins of time are chosen differently for each case (arb. orig.). Green and red circles represent reversal starts and ends, respectively.

figure 4(*d*) ($\langle\tau\rangle \approx 60.7 \pm 7.5t_E$) and $h_c = 0.45$ shown in figure 4(*f*) ($\langle\tau\rangle \approx 68.5 \pm 8.5t_E$), no clear difference in the reversal events can be observed as compared to the no-control case shown in figure 4(*a*) ($\langle\tau\rangle_0 \approx 62.9 \pm 8.0t_E$). For $h_c = 0.3$ shown in figure 4(*e*) ($\langle\tau\rangle \approx 85.9 \pm 11.0t_E$), the number of reversal events becomes much less and the flow reversals are suppressed.

In order to characterize the control effect quantitatively, we plot in figure 5 $\langle\tau_-\rangle/\langle\tau\rangle_0$ and $\langle\tau_+\rangle/\langle\tau\rangle_0$ for the two-point control and $\langle\tau\rangle/\langle\tau\rangle_0$ for the four-point control from the 2-D and quasi-2-D simulations at $Ra = 10^8$ and $Pr = 2$ with different h_c. Here, $\langle\tau\rangle_0$ is the mean time interval between successive reversals from the no-control case. As discussed above, due to the symmetry-breaking property of the two-point control configuration, the system will prefer a certain LSC orientation, and thus $\langle\tau_-\rangle$ and $\langle\tau_+\rangle$ will be different and they are obtained separately. The overall $\langle\tau\rangle = (\langle\tau_-\rangle + \langle\tau_+\rangle)/2$ at different h_c are listed in table 1 and will not be shown here. If the reversals are fully eliminated, $\langle\tau\rangle$ would be infinity and they will not be shown with symbols in figure 5.

For the 2-D cavity shown in figure 5(*a*), it is evident that both the two-point and four-point controls can suppress the flow reversal effectively for $0 \le h_c \le 0.45$. For the two-point control configuration, the sidewall control can fully eliminate the flow reversal when $0.05 \le h_c \le 0.4$, and it will make the system favour the clockwise LSC orientation when $h_c = 0.45$. For the four-point control, the control can also fully eliminate the flow reversal when $0.1 \le h_c \le 0.4$, and it can result in a stronger reversal suppression for $h_c = 0.05$ than for $h_c = 0.45$. For the quasi-2-D cavity shown in figure 5(*b*), the sidewall control may not be so effective as those in a 2-D cavity for both configurations. The two-point control with $h_c > 0$ can suppress the flow reversals again and the system favours the clockwise LSC orientation since $\langle\tau_-\rangle/\langle\tau\rangle_0 > \langle\tau_+\rangle/\langle\tau\rangle_0$. The value of $\langle\tau_-\rangle/\langle\tau\rangle_0$ generally

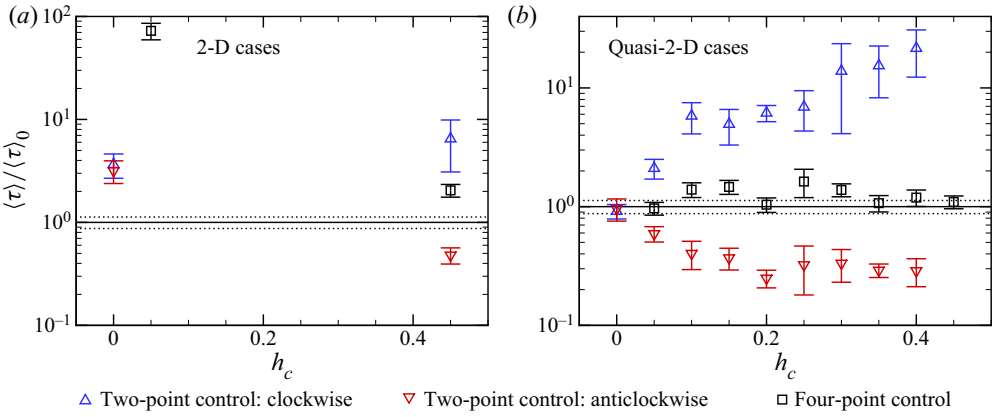

Figure 5. Plots of $\langle\tau_-\rangle/\langle\tau\rangle_0$ and $\langle\tau_+\rangle/\langle\tau\rangle_0$ for the two-point control and $\langle\tau\rangle/\langle\tau\rangle_0$ for the four-point control from the (*a*) 2-D and (*b*) quasi-2-D simulations at $Ra = 10^8$ and $Pr = 2$ with $0 \le h_c \le 0.45$. Here $\langle\tau\rangle_0$ is the mean time interval between successive reversals from the no-control case. Dotted lines represent the error bars of $\langle\tau\rangle_0$. Symbols $\triangle$ and $\triangledown$ denote $\langle\tau_-\rangle$ and $\langle\tau_+\rangle$ in the two-point control configuration, respectively. If the reversals are fully eliminated at certain h_c, there will be no symbol shown.

increases with h_c and the reversals are fully suppressed when $h_c = 0.45$, indicating that the two-point control is more effective in suppressing the flow reversal when h_c is larger. For the four-point control, it can generally suppress the flow reversal very mildly when $0.1 \le h_c \le 0.45$, but the suppression effect is not monotonic with h_c as is the two-point control and the efficiency is relatively lower. With $h_c = 0.1$, 0.15, 0.25 and 0.3, the control can suppress the flow reversal considerably.

Figure 6 shows the temperature contours, the in-plane velocity vectors and the in-plane $\boldsymbol{F}^b$ vectors (F_x^b, F_y^b) from instantaneous flow fields with the two-point control and four-point control configurations in 2-D and quasi-2-D cavities. Here, $\boldsymbol{F}^b = (F_x^b, F_y^b, F_z^b) = \theta\boldsymbol{j} - \boldsymbol{\nabla} p_\theta$ is the divergence-free projection of the buoyancy force, with p_θ being the pressure required to eliminate the divergence of the buoyancy force (Zhang *et al.* 2020):

$$\nabla^2 p_\theta = \partial\theta/\partial y, \quad \partial p_\theta/\partial x|_{x=\pm 0.5} = \partial p_\theta/\partial z|_{z=\pm 0.15} = 0, \quad \partial p_\theta/\partial y|_{y=\pm 0.5} = \theta. \tag{3.1a–c}$$

From the momentum equation, it can be inferred that $\boldsymbol{F}^b$ is the only source for the control region to instantly influence the evolution of the velocity field. As shown in figure 6(*a*3,*b*3,*c*3,*d*3), the hot plume with $\theta > 0$ rising along the right sidewall may contact with the local zone with $\theta \approx 0$ and result in a local $\partial\theta/\partial y < 0$ zone close to the control area. The negative $\partial\theta/\partial y$ appears as the source term in (3.1*a–c*), which contributes positively to $\partial p_\theta/\partial x$ and thus negatively to F_x^b on the left side of this $\partial\theta/\partial y < 0$ region, according to the Green's function. Similarly, when a cold plume descending along the right sidewall meets with the control region (see figure 6*b*2,*d*2), there would also be a local region contributing negatively to F_x^b. In other words, when a descending cold plume or rising hot plume meets with the control region on a sidewall, the resulting negative $\partial\theta/\partial y$ tends to force $\boldsymbol{F}^b$ to point away from the corresponding sidewall. Therefore, the control region tends to drive any plume it touches to separate, and thus weakens or restrains the corresponding vortex (LSC or corner rolls) fed by the plume. Another effect of control

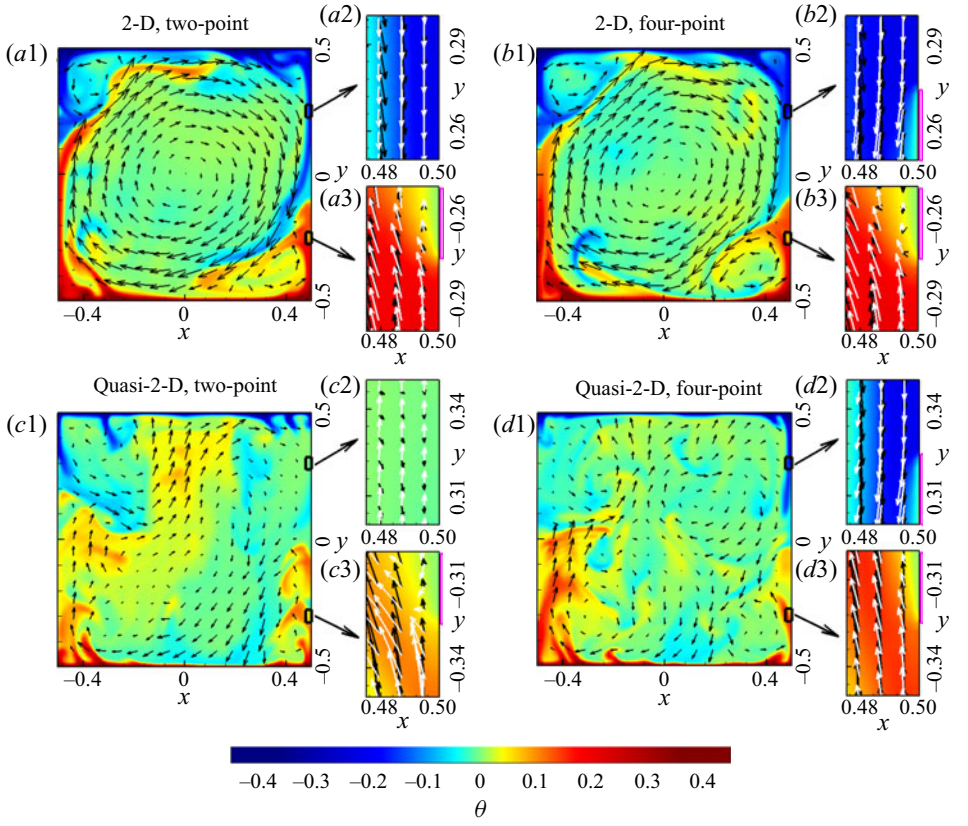

Figure 6. Temperature contours (colour), in-plane velocity vectors (black) and in-plane $\boldsymbol{F}^b$ vectors (white) of instantaneous fields in the $z = 0$ plane. The lengths of the vectors are proportional to their magnitudes. The control parameters are $Ra = 10^8$ and $Pr = 2$. Panels: ($a1$,$a2$,$a3$) 2-D and two-point control, $h_c = 0.25$, $t_E = 2.5 \times 10^3$; ($b1$,$b2$,$b3$) 2-D and four-point control, $h_c = 0.25$, $t_E = 3.5 \times 10^3$; ($c1$,$c2$,$c3$) quasi-2-D and two-point control, $h_c = 0.3$, $t_E = 3.5 \times 10^3$; ($d1$,$d2$,$d3$) quasi-2-D and four-point control, $h_c = 0.3$, $t_E = 0.7 \times 10^3$. Panels ($a1$,$b1$,$c1$,$d1$) show the temperature contours and in-plane velocity vectors in the whole domain; ($a2$,$b2$,$c2$,$d2$) show the zoomed-in temperature contours, in-plane velocity vectors (black) and in-plane $\boldsymbol{F}^b$ vectors (white) near the upper-right control region (if it exists); ($a3$,$b3$,$c3$,$d3$) show the zoomed-in temperature contours, in-plane velocity vectors (black) and in-plane $\boldsymbol{F}^b$ vectors (white) near the lower-right control region.

regions on the vortices is to reduce the $|\theta|$ of plumes through thermal conduction, and consequently to reduce the $v\theta$, which is the production term of kinetic energy.

In all, the control region has two approaches to restrain or weaken a vortex that it contacts with, either through the instant $\boldsymbol{F}^b$ or through the slow thermal conduction. Specifically, if a control region contacts with the LSC, it will weaken the LSC and implicitly provide more opportunity for the growth of corner rolls, motivating the LSC to reverse. If the control region contacts with a corner roll, it will suppress the growth of the corner roll and implicitly strengthen the LSC, which helps to stabilize the LSC. For a clockwise state and $h_c > 0$, the two control regions in the second and fourth quadrants from both control configurations would weaken the corner roll when they grow large enough, but the two extra control regions in the first and third quadrants from the four-point control would weaken the LSC. Therefore, the clockwise LSC is less stable under the four-point control as compared to the two-point control. For an anticlockwise state and

$h_c > 0$, the two control regions in the second and fourth quadrants from both control configurations would weaken the LSC, but the two extra control regions in the first and third quadrants from the four-point control would weaken the corner rolls when they grow large enough. Therefore, the anticlockwise LSC is more stable under the four-point control as compared to the two-point control.

The difference between the 2-D and quasi-2-D cavities, in the h_c range of two-point control for efficient reversal suppression, can also be explained with figure 6. Figure 6(a1,c1) suggests that both the LSC and corner rolls are weaker in a quasi-2-D cavity when they are compared to those in a 2-D cavity, resulting in the plumes being less likely to keep rising or descending along sidewalls. For the two-point control in a quasi-2-D cavity, larger h_c makes control regions closer to horizontal plates, easier to contact with plumes from the corners, and thus more efficient in reversal suppression. On the other hand, the forcing effect is not dominant for the two-point control with a medium h_c in a quasi-2-D cavity. In a 2-D cavity, when a plume feeding the corner rolls is forced to separate from the sidewall, it will probably be pressed by the strong LSC, heading towards the horizontal plate where the plume originates from (see figure 6a1,a3). However, in a quasi-2-D cavity, the plume could usually maintain its vertical movement after being forced by the control region (see figure 6c1,c3), since the LSC might be too weak to force it to turn back.

The concept of symmetry is also helpful in explaining the stabilizing/destabilizing effect of sidewall control on LSC. According to Huang *et al.* (2015), a more symmetric boundary condition may require more frequent reversals to restore the symmetry. In order to properly define symmetry, variable transformations should be first defined as follows (Podvin & Sergent 2015; Castillo-Castellanos *et al.* 2019):

$$\left.\begin{aligned} \mathcal{S}_x\colon\quad & [\tilde{u},\tilde{v},\tilde{w},\tilde{\theta}](x,y,z,t) = [-u,+v,+w,+\theta](-x,+y,+z,+t),\\ \mathcal{S}_y\colon\quad & [\tilde{u},\tilde{v},\tilde{w},\tilde{\theta}](x,y,z,t) = [+u,-v,+w,-\theta](+x,-y,+z,+t),\\ \mathcal{R}_\pi\colon\quad & [\tilde{u},\tilde{v},\tilde{w},\tilde{\theta}](x,y,z,t) = [-u,-v,+w,-\theta](-x,-y,+z,+t). \end{aligned}\right\} \tag{3.2}$$

Here, $\mathcal{S}_x$ represents the reflection about plane $x = 0$, $\mathcal{S}_y$ represents the reflection about plane $y = 0$, and $\mathcal{R}_\pi = \mathcal{S}_x\mathcal{S}_y = \mathcal{S}_y\mathcal{S}_x$ represents the 180° rotation about line $x = y = 0$. The symmetry property of the boundary conditions could be defined accordingly. Straightforwardly, a system that behaves according to both the symmetry $\mathcal{S}_x$ and $\mathcal{S}_y$ behaves according to the symmetry $\mathcal{R}_\pi$ automatically, while the symmetry $\mathcal{R}_\pi$ could not guarantee the symmetry $\mathcal{S}_x$ nor $\mathcal{S}_y$.

Since the Dirichlet boundary condition applies a stronger constraint to a system as compared to the Neumann boundary condition, the type and level of symmetry would be greatly influenced by the sidewall control. In Zhang *et al.* (2020), a similar explanation as in Huang *et al.* (2015) was given to interpret the results in 2-D geometry. For the two-point control with $h_c = 0$, the symmetry $\mathcal{S}_x$ and symmetry $\mathcal{S}_y$ of the system are enhanced and the reversals are consequently enhanced, while for the two-point control with $h_c \neq 0$ only the symmetry $\mathcal{R}_\pi$ is maintained while the symmetry $\mathcal{S}_x$ and symmetry $\mathcal{S}_y$ are broken. Thus the system prefers a certain orientation of LSC and correspondingly the reversal is suppressed or eliminated. However, a higher $Ra = 10^8$ changes the results and the two-point control with $h_c = 0$ can suppress the reversals in 2-D simulations. In addition, the newly introduced four-point control, which also satisfies $\mathcal{S}_x$, $\mathcal{S}_y$ and $\mathcal{R}_\pi$ symmetry, could also suppress reversals with proper h_c. Therefore, it is important to realize that the RBC is not always ergodic, and a system with more symmetric boundary condition does not always have the 'intention' to reach corresponding symmetries statistically.

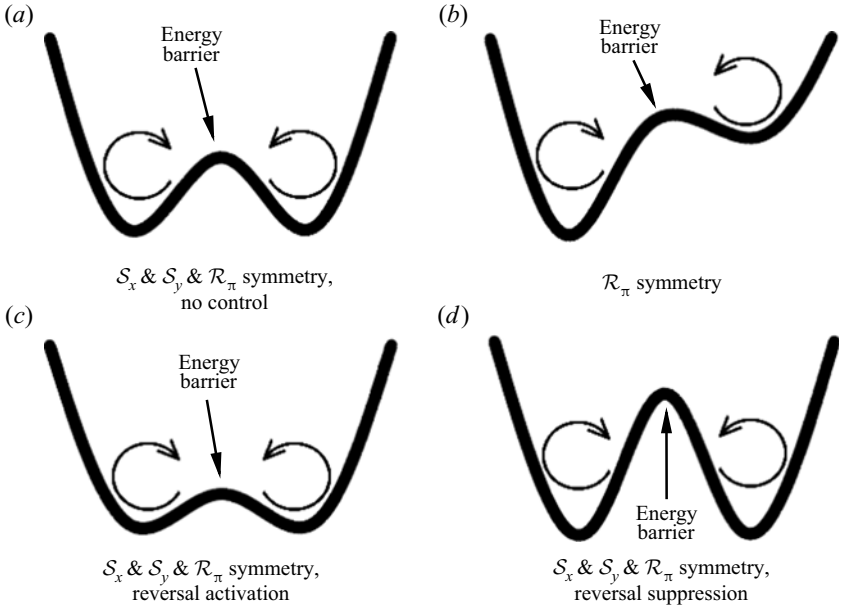

Figure 7. Conceptual energy curves of dynamical picture demonstrating reversal suppression/activation effect: (*a*) $\mathcal{S}_x$, $\mathcal{S}_y$ and $\mathcal{R}_\pi$ symmetry, corresponding to the 'no-control' case; (*b*) $\mathcal{R}_\pi$ symmetry, corresponding to the present two-point control cases with $h_c \geq 0.05$; (*c*) $\mathcal{S}_x$, $\mathcal{S}_y$ and $\mathcal{R}_\pi$ symmetry, corresponding to the reversal-enhancing cases with the two-point $h_c = 0$ control and the four-point control; and (*d*) $\mathcal{S}_x$, $\mathcal{S}_y$ and $\mathcal{R}_\pi$ symmetry, corresponding to the reversal-suppressing cases with the two-point $h_c = 0$ control and the four-point control.

With the results above, a more reasonable dynamical picture, which is similar to that in Sreenivasan *et al.* (2002), is introduced to demonstrate the reversal suppression/activation effect of sidewall control. Figure 7 shows the conceptual energy curves corresponding to different symmetry, control configurations and flow states. The two concave parts of each curve represent the two metastable clockwise and anticlockwise LSC states (potential wells) where the system tends to stay, and the bulge in the middle of each curve represents the energy barrier that keeps the system from shifting between the two main states (Sreenivasan *et al.* 2002). Compared to figure 7(*a*), where no control is applied and the system behaves according to the symmetry $\mathcal{S}_x$, $\mathcal{S}_y$ and $\mathcal{R}_\pi$, figure 7(*b*) is asymmetric and corresponds to the system with two-point $h_c > 0$ control, which violates the symmetry $\mathcal{S}_x$ and $\mathcal{S}_y$ while only satisfying the $\mathcal{R}_\pi$ symmetry. The energy gap where the system intends to shift from the clockwise state to the anticlockwise state is higher than that for the system to shift from the anticlockwise state to the clockwise state, indicating the system's strong preference for the clockwise state. The energy gap on the two sides of the energy barrier depends on the value of h_c and δ_c. Figure 7(*c*,*d*) could both represent the $h_c = 0$ control and four-point control which satisfy the symmetry $\mathcal{S}_x$, $\mathcal{S}_y$ and $\mathcal{R}_\pi$. However, the energy barrier could be relatively lower or higher than that in figure 7(*a*), which depends on the specific flow state and control parameter, as discussed above. For example, the four-point control with $h_c = 0.25$ in the 2-D case at $Ra = 10^8$ and $Pr = 2$ could strongly limit the growth of corner rolls and greatly increase the energy barrier, and thus corresponds to figure 7(*d*).

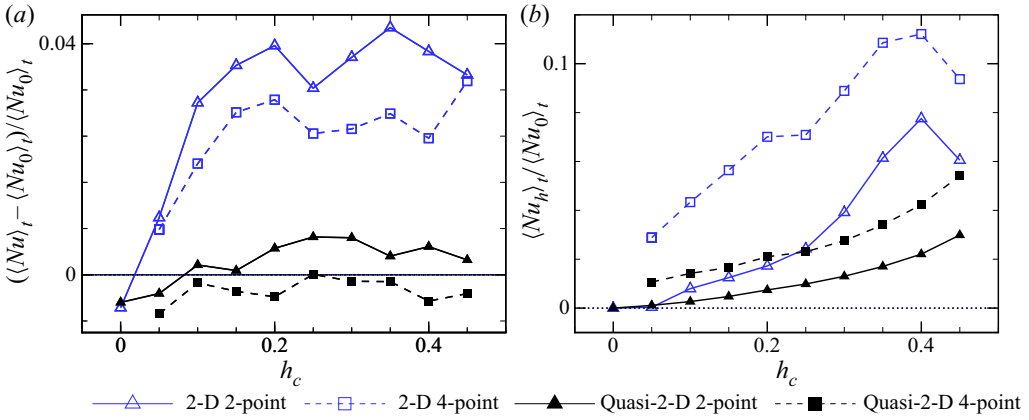

Figure 8. Relative time-averaged values of vertical and horizontal Nusselt numbers given by the 2-D and quasi-2-D simulations at $Ra = 10^8$ and $Pr = 2$. Here $\langle Nu_0\rangle_t$ denotes the vertical Nusselt number without sidewall control. (*a*) Relative time-averaged vertical Nusselt number difference $(\langle Nu\rangle_t - \langle Nu_0\rangle_t)/\langle Nu_0\rangle_t$. (*b*) Relative time-averaged horizontal Nusselt number $\langle Nu_h\rangle_t/\langle Nu_0\rangle_t$.

3.2. *Heat transfer and kinetic energy*

Owing to the sidewall control, the heat transfer through the walls occurs in two different directions, the vertical one through horizontal plates and the horizontal one through the sidewalls. The former could be quantified by the Nusselt number,

$$Nu(t) = -\frac{1}{2}\left\langle \left.\frac{\partial\theta}{\partial y}\right|_{y=-0.5} + \left.\frac{\partial\theta}{\partial y}\right|_{y=0.5}\right\rangle_{x,z}, \tag{3.3}$$

while the latter could be quantified by the Nusselt number in the horizontal direction, which can be defined similarly as

$$\begin{aligned} Nu_h(t) &= \frac{1}{2}\left\langle \int_0^{0.5}\left(\left.\frac{\partial\theta}{\partial x}\right|_{x=0.5} - \left.\frac{\partial\theta}{\partial x}\right|_{x=-0.5}\right)\mathrm{d}y - \int_{-0.5}^{0}\left(\left.\frac{\partial\theta}{\partial x}\right|_{x=0.5} - \left.\frac{\partial\theta}{\partial x}\right|_{x=-0.5}\right)\mathrm{d}y\right\rangle_z \\ &= \frac{1}{2}\left[\left\langle \mathrm{sgn}(y)\frac{\partial\theta}{\partial x}\right\rangle_{y,z}\right|_{x=0.5} - \left\langle \mathrm{sgn}(y)\frac{\partial\theta}{\partial x}\right\rangle_{y,z}\Big|_{x=-0.5}\Bigg]. \end{aligned} \tag{3.4}$$

Here $\langle Nu_h\rangle_t$ denotes the heat absorbed by the control regions below the line $y = 0$ and also the heat injected by the control regions above the line $y = 0$. For the two-point control, the definition of Nu_h is consistent with that defined in Zhang *et al.* (2020). The time-averaged vertical Nusselt numbers $\langle Nu\rangle_t$ for the 2-D and quasi-2-D cases without sidewall control at $Ra = 10^8$ and $Pr = 2$ are 24.9 and 32.7, respectively, and they will be denoted as $\langle Nu_0\rangle_t$. The relative values of $\langle Nu\rangle_t$ and $\langle Nu_h\rangle_t$ normalized with the corresponding $\langle Nu_0\rangle_t$ are shown in figure 8.

According to the results shown in figure 8(*a*), the two-point control can enhance vertical heat transfer with $h_c \geq 0.1$ in both 2-D and quasi-2-D cavities. However, the enhancement of vertical heat transfer is limited, with a maximum 4.3 % increase of $(\langle Nu\rangle_t - \langle Nu_0\rangle_t)/\langle Nu_0\rangle_t$ at $h_c = 0.35$ in the 2-D cavity, and a maximum 0.6 % increase at $h_c = 0.25$ in the quasi-2-D cavity. The curves in figure 8(*a*) are non-monotonic, which is similar to the phase diagram of $\langle Nu\rangle_t$ in Zhang *et al.* (2020), indicating that the underlying

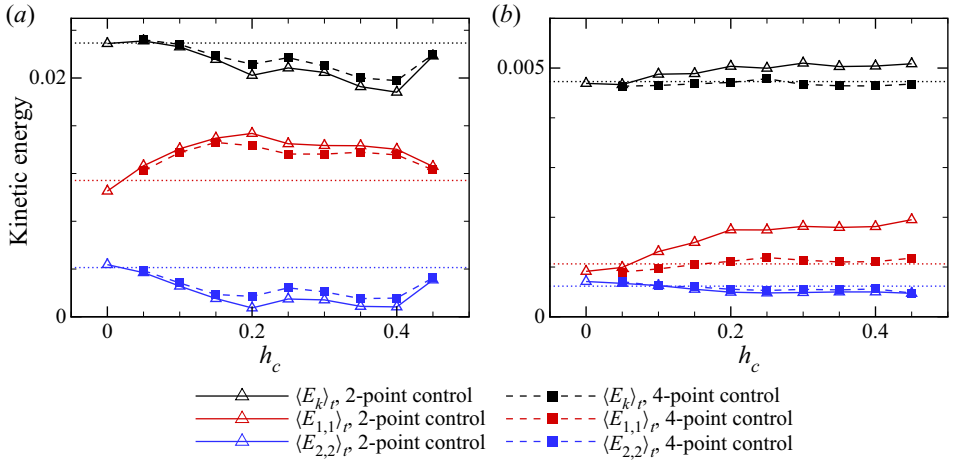

Figure 9. Time-averaged kinetic energy and the corresponding contribution from (1, 1) and (2, 2) modes, in 2-D and quasi-2-D cases with $Ra = 10^8$ and $Pr = 2$: (*a*) 2-D cases and (*b*) quasi-2-D cases in the $z = 0$ plane. The three dotted lines denote the corresponding time-averaged kinetic energy (black) and the contributions from the modes (1, 1) (red) and (2, 2) (blue) for the case without sidewall control.

mechanism of the vertical heat transfer enhancement/suppression caused by control is rather complicated. Nevertheless, the reduction of vertical heat transfer by $h_c = 0$ could be explained by larger corner rolls and consequently weaker LSC caused by control points at $y = 0$, which is also indicated by figure 9. The four-point control is generally less capable of promoting vertical heat transport in both 2-D and quasi-2-D cavities, with significantly lower values of $(\langle Nu\rangle_t - \langle Nu_0\rangle_t)/\langle Nu_0\rangle_t$ than the corresponding two-point control cases. In the quasi-2-D cases, it is shown that the four-point control can even suppress heat transfer. Based on the above results for $\langle Nu\rangle_t$ and the mean time intervals between successive reversals shown in figure 5, we would like to suggest the two-point control with $0.1 \leq h_c \leq 0.45$ for the 2-D cavities and $0.2 \leq h_c \leq 0.45$ for the quasi-2-D cavities.

As shown in figure 8(*b*), $\langle Nu_h\rangle_t$ are generally larger than zero and mostly increasing with h_c. With heat conduction mainly with plumes in the corner rolls, the two-point control could achieve a relative $\langle Nu_h\rangle_t$ of 7.8 % at $h_c = 0.4$ in the 2-D cavity, and 3.0 % at $h_c = 0.45$ in the quasi-2-D cavity. The $\langle Nu_h\rangle_t$ of the four-point control is always larger than that of the corresponding two-point control. This is as expected, since there are two more control regions so that the plumes feeding corner rolls and the plumes feeding the LSC are all conducting heat with control regions, increasing the heat transfer through the sidewalls. From $h_c = 0.4$ to $h_c = 0.45$, the $\langle Nu_h\rangle_t$ decreased in 2-D geometry for both two-point and four-point control, although the control regions are closer to horizontal plates and surrounded by fluids with larger $|\theta|$. This is mainly because the velocity of corner rolls on the sidewalls at $y \approx \pm 0.45$ is relatively smaller and limits the heat transfer.

Besides heat transfer, the kinetic energy is also important in the dynamics of RBC flow. Here 2-D motion characterized by the (u, v) field in the $z = 0$ plane is investigated, in a way similar to the analysis of the particle image velocimetry result in experiments (Chen *et al.* 2019). The plane-averaged kinetic energy of (u, v) is defined as $E_k(t) \triangleq \langle u(x, y, 0, t)^2 + v(x, y, 0, t)^2\rangle_{x,y}/2$. In order to demonstrate the distribution of E_k from

different scales, Fourier modes could be defined in the x–y plane (Chen *et al.* 2019) as

$$\left.\begin{aligned} u^{m,n} &= 2\sin(m\pi\tilde{x})\cos(n\pi\tilde{y}), \\ v^{m,n} &= -2\cos(m\pi\tilde{x})\sin(n\pi\tilde{y}), \end{aligned}\right\} \tag{3.5}$$

with $\tilde{x} \triangleq x + 0.5$ and $\tilde{y} \triangleq y + 0.5$. The expansion coefficients of $u(x, y, 0, t)$ and $v(x, y, 0, t)$ have certain expressions:

$$\left.\begin{aligned} A_u^{m,n}(t) &= \langle u(x, y, 0, t)u^{m,n}\rangle_{x,y}, \\ A_v^{m,n}(t) &= \langle v(x, y, 0, t)v^{m,n}\rangle_{x,y}. \end{aligned}\right\} \tag{3.6}$$

Therefore, the kinetic energy contributed by the (m, n) mode of u and v should be

$$E_{m,n}(t) = ([A_u^{m,n}(t)]^2 + [A_v^{m,n}(t)]^2)/2. \tag{3.7}$$

The kinetic energy $E_k(t)$ together with the shares contributed by the (1, 1) and (2, 2) modes in the 2-D and quasi-2-D cases with $Ra = 10^8$ and $Pr = 2$ are averaged in time and shown in figure 9. For the 2-D cases, the two-point and four-point control configurations with $h_c \geq 0.1$ would reduce the kinetic energy $\langle E_k\rangle_t$, with a maximum reduction up to approximately 18.0 % for the two-point control, accompanied by a maximum reduction up to 82.1 % for $\langle E_{2,2}\rangle_t$. However, the reduction of the kinetic energy does not reduce, but enhances, the heat transfer in the vertical direction, as seen from figure 8(*a*). This is because the control with $h_c \geq 0.1$ could significantly enhance the LSC strength characterized by $\langle E_{1,1}\rangle_t$, the contribution to the kinetic energy from the (1, 1) mode, which is increased by up to 35 % as shown in figure 9(*a*). Since the large-scale LSC is more efficient in carrying heat between horizontal plates, the enhancement of LSC should be the main reason for the enhancement of heat transfer seen in figure 8(*a*) even though the kinetic energy is reduced. This explanation is also valid for the two-point control with $h_c = 0$, where the reduction of $E_{1,1}$ is accompanied by a reduction of $\langle Nu\rangle_t$, although the total kinetic energy is almost unchanged.

Unlike the 2-D cases, for the quasi-2-D cases, the two-point control with $h_c \geq 0.1$ could increase the total kinetic energy, with a maximum increase of 7.8 % at $h_c = 0.3$, while the four-point control might reduce it slightly in general. With the two-point control and $h_c > 0.1$, $\langle E_{1,1}\rangle_t$ could significantly increase by up to 83.6 % at $h_c = 0.45$, while there is a slight decrease of $\langle E_{2,2}\rangle_t$. The domination of the (1, 1) mode over the (2, 2) mode could be an important reason for reversal suppression, which can also be inferred from figure 10(*a*,*b*), where the LSC, being squeezed by corner rolls in the no-control case, could become larger with the two-point control and $h_c = 0.3$. As mentioned by Chen *et al.* (2019), in quasi-2-D convection, a slimmer LSC is convenient for corner rolls to take over and thus increases the probability of flow reversal. Therefore, although the control could not effectively force the separation of plumes feeding the corner rolls, the weakening effect on corner rolls through thermal conduction could still lead to a more stable state with stronger LSC and weaker corner rolls.

Differently from those results in a 2-D cavity discussed above, the four-point control in a quasi-2-D cavity could not effectively enhance $\langle E_{1,1}\rangle_t$, and its value at different h_c oscillates around the reference value from the case without sidewall control. We may conclude that the LSC with four-point control has not been strengthened significantly in a quasi-2-D cavity, as shown in figure 10(*c*) with $h_c = 0.3$, and thus the heat transfer in the vertical direction is comparable to (slightly less than) that from the case with adiabatic sidewalls. On the other hand, the mild decrease of $\langle E_{2,2}\rangle_t$ and almost unchanged $\langle E_{1,1}\rangle_t$,

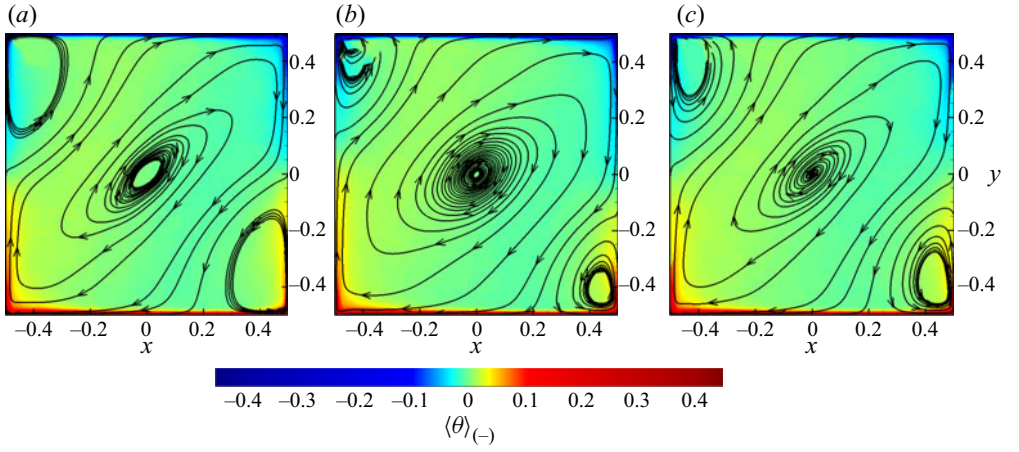

Figure 10. Temperature contours and in-plane streamlines of fields in the $z = 0$ plane and averaged during clockwise state between reversals in quasi-2-D cases with $Ra = 10^8$ and $Pr = 2$: (*a*) no control; (*b*) two-point control with $h_c = 0.3$; and (*c*) four-point control with $h_c = 0.3$.

as compared to the no-control case, are consistent with the slight increase of the mean time interval between successive reversals as shown in figure 5(*b*), which corresponds to the slight suppression of flow reversals with the four-point control in a quasi-2-D cavity.

4. Experimental and numerical results at higher *Ra* and *Pr*

In § 3, we have shown the numerical results at $Ra = 10^8$ and $Pr = 2$ in 2-D and quasi-2-D cavities with different control configurations and found that the two-point control with $h_c > 0$ can effectively suppress the flow reversals in both 2-D and quasi-2-D cavities while the four-point control can effectively suppress the flow reversals only in the 2-D cavity. In this section, we will investigate the two-point control with $h_c = 0$ and $h_c = 0.15$ in the quasi-2-D cavity at higher Ra and Pr numerically and experimentally.

Figure 11 shows the time series of $\hat{\delta}(t)$ from the two-point controlled quasi-2-D experiments with $h_c = 0$ and $h_c = 0.15$ at $Ra \approx 1.93 \times 10^8$ and $Pr = 5.7$ as well as from the corresponding no-control case. It is seen that flow reversals happen frequently in a $600t_E$ time span when the sidewalls are adiabatic (without control), while the number of flow reversals reduces obviously for the two-point control with $h_c = 0$ and $h_c = 0.15$ in the same time span, indicating the effective suppression of flow reversals from the two-point control with $h_c = 0$ and $h_c = 0.15$. Our numerical results show a similar trend with increasing $\langle\tau\rangle$ for the two-point control with $h_c = 0$ and $h_c = 0.15$, as listed in table 2.

Furthermore, for the two-point control with $h_c = 0$ and the no-control case, the system seems to stay in the clockwise and anticlockwise states equally, while it shows a strong preference for the clockwise state for the two-point control with $h_c = 0.15$. The $\langle\tau\rangle$ values from the no-control cases and the two-point control cases with $h_c = 0$, as well as $\langle\tau_-\rangle$ and $\langle\tau_+\rangle$ from the two-point control cases with $h_c = 0.15$ at different Ra are obtained and shown in figure 12. It is evident that the two-point control with $h_c = 0.15$ could significantly suppress the flow reversals and favours the clockwise state, while the two-point control with $h_c = 0$ can either suppress or enhance the flow reversals in the quasi-2-D experiments. At two lower Ra ($Ra = 1.92 \times 10^8$ and 2.71×10^8), the experimental results show that the two-point control with $h_c = 0$ can slightly suppress the

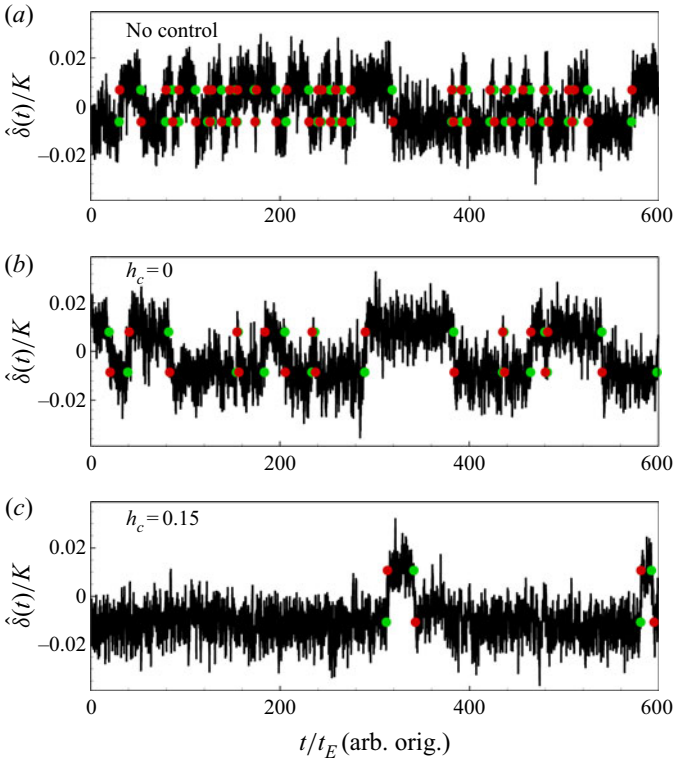

Figure 11. Plots of $\hat{\delta}(t)$ of quasi-2-D experiments at $Ra \approx 1.93 \times 10^8$ and $Pr = 5.7$ with two-point control or without control: (*a*) no control; (*b*) two-point control with $h_c = 0$; and (*c*) two-point control with $h_c = 0.15$. Green and red circles represent reversal starts and ends respectively.

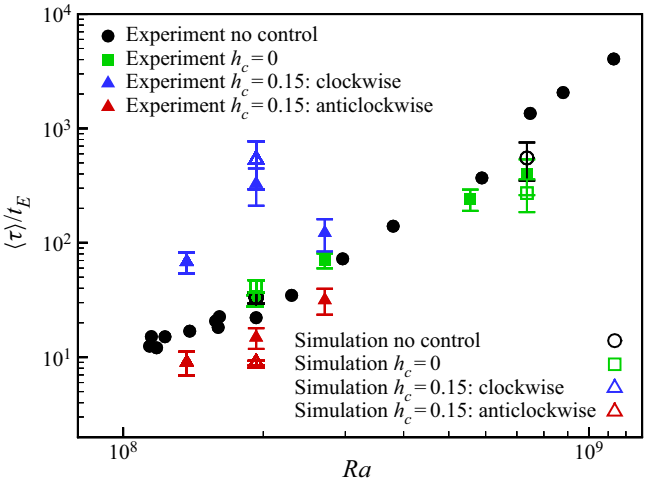

Figure 12. Mean reversal intervals from quasi-2-D experiments and simulations with two-point control configuration and without control at $Pr = 5.7$. Experimental data of no-control cases are obtained from Chen *et al.* (2019).

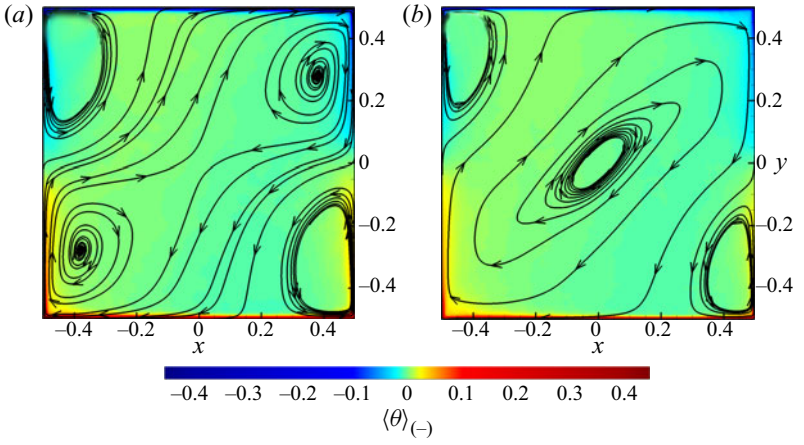

Figure 13. Averaged temperature contours and in-plane streamlines of fields in the $z = 0$ plane from the simulations of the no-control quasi-2-D cases with $Pr = 5.7$: (*a*) $Ra = 1.93 \times 10^8$ and (*b*) $Ra = 7.36 \times 10^8$. The averaging is performed on the condition that the system is in the clockwise state.

reversal, while at two higher Ra ($Ra = 5.56 \times 10^8$ and 7.36×10^8), it is shown that the control can enhance the flow reversal.

Simulation results show good consistency with the experiments, although their definitions of t_E are different. The relative reversal suppression/enhancement for $h_c = 0$ control are very close between simulations and experiments at both $Ra = 1.93 \times 10^8$ and $Ra = 7.36 \times 10^8$. However, for two-point control with $h_c = 0.15$, the clockwise state seems to exhibit greater predominance over the anticlockwise state from the simulation than the experiment at $Ra = 1.93 \times 10^8$. This is probably because the copper blocks have non-zero thermal resistance, which would not realize isothermal boundary conditions perfectly and would have less weakening effect on corner rolls as expected. Nevertheless, the experiments have proved that simply increasing thermal conductivity locally on sidewalls would have significant influence on LSC stability.

Now, we are going to explain why the two-point control with $h_c = 0$ behaves differently at $Ra = 1.93 \times 10^8$ and 7.36×10^8. Chen *et al.* (2019) observed a new, less stable, abnormal single-roll state with substructures inside the single roll when Ra decreases from a high value, where the classic single-roll state exists, to a relative low value, where a four-roll state can be observed. With $Pr = 5.7$, the transition Ra from the single-roll state to the abnormal single-roll state is around 2.1×10^8. Figure 13 shows the averaged temperature contours and the in-plane streamlines of flow fields in the $z = 0$ plane from the no-control cases with $Ra = 1.93 \times 10^8$ and $Ra = 7.36 \times 10^8$, and it is seen that the system shows the abnormal single-roll state at $Ra = 1.93 \times 10^8$, while it reveals the single-roll state at $Ra = 7.36 \times 10^8$, which are consistent with the experimental results in Chen *et al.* (2019). According to Chen *et al.* (2020), the reversal of the abnormal single-roll state is dominated by the instability of LSC, which is highly squeezed to be dumbbell-shaped by the corner rolls. Since the structural stability of LSC is already low for the abnormal single-roll state, the $h_c = 0$ control may not further reduce the LSC stability, but could instead reduce the perturbations on LSC from plumes, resulting in a suppression of reversals. When Ra is higher and the flow turns into the single-roll state, whose reversal is dominated by the growth of corner rolls (Chen *et al.* 2020), the presence of $h_c = 0$ control

could raise the height of the corner rolls and increase the instability of LSC, consequently enhancing reversals.

5. Conclusion

In the present paper, the local sidewall control on 2-D and quasi-2-D RBC is studied numerically and experimentally. In addition to the two-point control configuration studied by Zhang *et al.* (2020), another configuration with four control regions and higher symmetry property is also simulated and compared with those two-point control cases. With a fixed width of the control region $\delta_c = 0.05$ at $Ra = 10^8$ and $Pr = 2$, the direct numerical simulation results show that both the two-point and four-point controls can effectively suppress the flow reversals when $h_c \geq 0.05$ in the 2-D cavity, while only the two-point control shows effective suppression on the flow reversal with $h_c \geq 0.05$ in the quasi-2-D cavity. The effect of the four-point control in the quasi-2-D cavity is rather limited. Further analysis shows that the two-point control with $h_c \geq 0.05$ will favour a clockwise LSC state over the anticlockwise LSC state in both 2-D and quasi-2-D cavities. In addition, the two-point control with $h_c \geq 0.1$ can significantly increase the energy of LSC according to the mode decomposition and consequently increase the vertical heat transfer. More specifically, in the 2-D cavity some medium h_c is optimal for reversal suppression, but in the quasi-2-D cavity larger h_c seems to be more efficient in reversal suppression. These results not only reveal the superior suppression effect of the two-point control over the four-point control, but also show the differences between 2-D and quasi-2-D simulations.

Besides the discussions on the reversal suppression/enhancement effect from different control configurations, a conceptual picture is presented based on symmetry: the two-point control with $h_c > 0$ breaks the symmetry about planes $x = 0$ and $y = 0$, and favours a specific LSC orientation; while $h_c = 0$ control and four-point control increase the level of symmetry but its suppression/enhancement on reversals should be decided together with specific flow state. Whether a symmetry-preserving control increases or reduces the LSC stability still remains an open question.

The effect of the two-point control at $Pr = 5.7$ with higher Ra up to 7.36×10^8 is also investigated in the quasi-2-D cavity, both numerically and experimentally, to explore the realizability and efficiency of the control strategy in real flows. Simulations and experiments with the same parameters show good consistency, suggesting that the present control strategy is practicable and efficient for real flow apparatus. Furthermore, the results show that the two-point control with $h_c = 0.15$ can effectively suppress the flow reversal while the two-point control with $h_c = 0$ can either suppress or activate the reversals depending on Ra. With fixed $Pr = 5.7$ and $Ra = 1.93 \times 10^8$, the control will suppress the flow reversals while it can activate the reversals at higher $Ra = 7.36 \times 10^8$. We attribute the discrepancies at different Ra to the different flow topology. Since the flow topology also depends on Pr, further studies may be performed to investigate the Pr and Ra effects on the two-point control with different h_c.

Acknowledgements. The numerical simulations were finished at National Supercomputer Center in Guangzhou (Tianhe-2A), China.

Funding. This work was supported by the National Science Foundation of China (NSFC grant nos. 11822208, 11988102, 11772297, 91852205, 11825204 and 11772259) and Shenzhen Science and Technology Program (grant no. KQTD20180411143441009).

Declaration of interest. The authors report no conflict of interest.

Author ORCIDs.
Shengqi Zhang https://orcid.org/0000-0001-8273-7484;
Xin Chen https://orcid.org/0000-0001-9373-9696;
Zhenhua Xia https://orcid.org/0000-0002-5672-5890;
Heng-Dong Xi https://orcid.org/0000-0002-2999-2694;
Quan Zhou https://orcid.org/0000-0002-0411-7228;
Shiyi Chen https://orcid.org/0000-0002-2913-4497.

References

Ahlers, G., Grossmann, S. & Lohse, D. 2009 Heat transfer and large scale dynamics in turbulent Rayleigh–Bénard convection. *Rev. Mod. Phys.* **81** (2), 503–537.

Araujo, F.F., Grossmann, S. & Lohse, D. 2005 Wind reversals in turbulent Rayleigh–Bénard convection. *Phys. Rev. Lett.* **95**, 084502.

Assaf, M., Angheluta, L. & Goldenfeld, N. 2011 Rare fluctuations and large-scale circulation cessations in turbulent convection. *Phys. Rev. Lett.* **107**, 044502.

Benzi, R. 2005 Flow reversal in a simple dynamical model of turbulence. *Phys. Rev. Lett.* **95**, 024502.

Brown, E. & Ahlers, G. 2007 Large-scale circulation model for turbulent Rayleigh–Bénard convection. *Phys. Rev. Lett.* **98**, 134501.

Brown, E. & Ahlers, G. 2008*a* Azimuthal asymmetries of the large-scale circulation in turbulent Rayleigh–Bénard convection. *Phys. Fluids* **20** (10), 105105.

Brown, E. & Ahlers, G. 2008*b* A model of diffusion in a potential well for the dynamics of the large-scale circulation in turbulent Rayleigh—Bénard convection. *Phys. Fluids* **20**, 075101.

Brown, E., Funfschilling, D. & Ahlers, G. 2007 Anomalous Reynolds-number scaling in turbulent Rayleigh–Bénard convection. *J. Stat. Mech.-Theory Exp.* **2007** (10), P10005.

Brown, E., Nikolaenko, A. & Ahlers, G. 2005 Reorientation of the large-scale circulation in turbulent Rayleigh–Bénard convection. *Phys. Rev. Lett.* **95**, 084503.

Castillo-Castellanos, A., Sergent, A., Podvin, B. & Rossi, M. 2019 Cessation and reversals of large-scale structures in square Rayleigh–Bénard cells. *J. Fluid Mech.* **877**, 922–954.

Chandra, M. & Verma, M.K. 2011 Dynamics and symmetries of flow reversals in turbulent convection. *Phys. Rev.* E **83**, 067303.

Chandra, M. & Verma, M.K. 2013 Flow reversals in turbulent convection via vortex reconnections. *Phys. Rev. Lett.* **110**, 114503.

Chen, X., Huang, S.-D., Xia, K.-Q. & Xi, H.-D. 2019 Emergence of substructures inside the large-scale circulation induces transition in flow reversals in turbulent thermal convection. *J. Fluid Mech.* **877**, R1.

Chen, X., Wang, D.-P. & Xi, H.-D. 2020 Reduced flow reversals in turbulent convection in the absence of corner vortices. *J. Fluid Mech.* **891**, R5.

Chong, K.L., Wagner, S., Kaczorowski, M., Shishkina, O. & Xia, K.-Q. 2018 Effect of Prandtl number on heat transport enhancement in Rayleigh–Bénard convection under geometrical confinement. *Phys. Rev. Fluids* **3**, 013501.

Cioni, S., Ciliberto, S. & Sommeria, J. 1997 Strongly turbulent Rayleigh—Bénard convection in mercury: comparison with results at moderate Prandtl number. *J. Fluid Mech.* **335**, 111–140.

van Doorn, E., Dhruva, B., Sreenivasan, K.R. & Cassella, V. 2000 Statistics of wind direction and its increments. *Phys. Fluids* **12** (6), 1529–1534.

Glatzmaiers, G.A. & Roberts, P.H. 1995 A three-dimensional self-consistent computer simulation of a geomagnetic field reversal. *Nature* **377** (6546), 203–209.

Grossmann, S. & Lohse, D. 2000 Scaling in thermal convection: a unifying theory. *J. Fluid Mech.* **407**, 27–56.

Grossmann, S. & Lohse, D. 2001 Thermal convection for large Prandtl numbers. *Phys. Rev. Lett.* **86**, 3316–3319.

Grossmann, S. & Lohse, D. 2002 Prandtl and Rayleigh number dependence of the Reynolds number in turbulent thermal convection. *Phys. Rev.* E **66**, 016305.

Hartmann, D.L., Moy, L.A. & Fu, Q. 2001 Tropical convection and the energy balance at the top of the atmosphere. *J. Climate* **14** (24), 4495–4511.

Huang, S.-D., Wang, F., Xi, H.-D. & Xia, K.-Q. 2015 Comparative experimental study of fixed temperature and fixed heat flux boundary conditions in turbulent thermal convection. *Phys. Rev. Lett.* **115**, 154502.

HUANG, S.-D. & XIA, K.-Q. 2016 Effects of geometric confinement in quasi-2-d turbulent Rayleigh–Bénard convection. *J. Fluid Mech.* **794**, 639–654.

KOOIJ, G., BOTCHEV, M., FREDERIX, E., GEURTS, B., HORN, S., LOHSE, D., VAN DER POEL, E., SHISHKINA, O., STEVENS, R.J. & VERZICCO, R. 2018 Comparison of computational codes for direct numerical simulations of turbulent Rayleigh–Bénard convection. *Comput. Fluids* **166**, 1–8.

LOHSE, D. & XIA, K.-Q. 2010 Small-scale properties of turbulent Rayleigh–Bénard convection. *Annu. Rev. Fluid Mech.* **42**, 335–364.

NI, R., HUANG, S.-D. & XIA, K.-Q. 2015 Reversals of the large-scale circulation in quasi-2D Rayleigh–Bénard convection. *J. Fluid Mech.* **778**, R5.

PETSCHEL, K., WILCZEK, M., BREUER, M., FRIEDRICH, R. & HANSEN, U. 2011 Statistical analysis of global wind dynamics in vigorous Rayleigh–Bénard convection. *Phys. Rev.* E **84**, 026309.

PODVIN, B. & SERGENT, A. 2015 A large-scale investigation of wind reversal in a square Rayleigh–Bénard cell. *J. Fluid Mech.* **766**, 172–201.

QIU, X.-L., XIA, K.-Q. & TONG, P. 2005 Experimental study of velocity boundary layer near a rough conducting surface in turbulent natural convection. *J. Turbul.* **6**, N30.

SREENIVASAN, K., BERSHADSKII, A. & NIEMELA, J.J. 2002 Mean wind and its reversal in thermal convection. *Phys. Rev.* E **65**, 056306.

STEVENS, R.J., LOHSE, D. & VERZICCO, R. 2014 Sidewall effects in Rayleigh–Bénard convection. *J. Fluid Mech.* **741**, 1–27.

SUGIYAMA, K., NI, R., STEVENS, R.J., CHAN, T.S., ZHOU, S.-Q., XI, H.-D., SUN, C., GROSSMANN, S., XIA, K.-Q. & LOHSE, D. 2010 Flow reversals in thermally driven turbulence. *Phys. Rev. Lett.* **105**, 034503.

SUN, C., XI, H.-D. & XIA, K.-Q. 2005 Azimuthal symmetry, flow dynamics, and heat transport in turbulent thermal convection in a cylinder with an aspect ratio of 0.5. *Phys. Rev. Lett.* **95**, 074502.

TSUJI, Y., MIZUNO, T., MASHIKO, T. & SANO, M. 2005 Mean wind in convective turbulence of mercury. *Phys. Rev. Lett.* **94**, 034501.

VAN DER POEL, E.P., OSTILLA-MÓNICO, R., DONNERS, J. & VERZICCO, R. 2015 A pencil distributed finite difference code for strongly turbulent wall-bounded flows. *Comput. Fluids* **116**, 10–16.

VASIL'EV, A. & FRICK, P.G. 2011 Reversals of large-scale circulation in turbulent convection in rectangular cavities. *J. Expl Theor. Phys.* **93**, 330–334.

WAGNER, S. & SHISHKINA, O. 2013 Aspect-ratio dependency of Rayleigh–Bénard convection in box-shaped containers. *Phys. Fluids* **25**, 085110.

WAN, Z.H., WEI, P., VERZICCO, R., LOHSE, D., AHLERS, G. & STEVENS, R.J. 2019 Effect of sidewall on heat transfer and flow structure in Rayleigh–Bénard convection. *J. Fluid Mech.* **881**, 218–243.

WANG, Q., XIA, S.-N., WANG, B.-F., SUN, D.-J., ZHOU, Q. & WAN, Z.-H. 2018 Flow reversals in two-dimensional thermal convection in tilted cells. *J. Fluid Mech.* **849**, 355–372.

WANG, Q., XU, B.-L., XIA, S.-N., WAN, Z.-H. & SUN, D.-J. 2017 Thermal convection in a tilted rectangular cell with aspect ratio 0.5. *Chin. Phys. Lett.* **34**, 104401.

WANG, B.-F., ZHOU, Q. & SUN, C. 2020 Vibration-induced boundary-layer destabilization achieves massive heat-transport enhancement. *Sci. Adv.* **6**, eaaz8239.

XI, H.-D. & XIA, K.-Q. 2007 Cessations and reversals of the large-scale circulation in turbulent thermal convection. *Phys. Rev.* E **75**, 066307.

XI, H.-D. & XIA, K.-Q. 2008 Azimuthal motion, reorientation, cessation, and reversal of the large-scale circulation in turbulent thermal convection: a comparative study in aspect ratio one and one-half geometries. *Phys. Rev.* E **78**, 036326.

XIA, S.-N., WAN, Z.-H., LIU, S., WANG, Q. & SUN, D.-J. 2016 Flow reversals in Rayleigh–Bénard convection with non-Oberbeck–Boussinesq effects. *J. Fluid Mech.* **798**, 628–642.

ZHANG, Y.-Z., SUN, C., BAO, Y. & ZHOU, Q. 2018 How surface roughness reduces heat transport for small roughness heights in turbulent Rayleigh–Bénard convection. *J. Fluid Mech.* **836**, R2.

ZHANG, S., XIA, Z., ZHOU, Q. & CHEN, S. 2020 Controlling flow reversal in two-dimensional Rayleigh–Bénard convection. *J. Fluid Mech.* **891**, R4.

ZHU, X., STEVENS, R.J.A.M., SHISHKINA, O., VERZICCO, R. & LOHSE, D. 2019 $Nu \sim Ra^{1/2}$ scaling enabled by multiscale wall roughness in Rayleigh–Bénard turbulence. *J. Fluid Mech.* **869**, R4.